Ferromagnetic domain behavior and phase transition in bilayer manganites investigated at the nanoscale

C. Phatak,[1,*] A. K. Petford-Long,[1,2] H. Zheng,[1] J. F. Mitchell,[1] S. Rosenkranz,[1] and M. R. Norman[1]
[1]*Materials Science Division, Argonne National Laboratory, 9700 South Cass Avenue, Argonne, Illinois 60439, USA*
[2]*Department of Materials Science and Engineering, Northwestern University, 2220 Campus Drive, Evanston, Illinois 60208, USA*
(Received 3 September 2015; revised manuscript received 17 October 2015; published 14 December 2015)

Understanding the underlying mechanism and phenomenology of colossal magnetoresistance in manganites has largely focused on atomic and nanoscale physics such as double exchange, phase separation, and charge order. Here we consider a more macroscopic view of manganite materials physics, reporting on the ferromagnetic domain behavior in a bilayer manganite sample with a nominal composition of $La_{2-2x}Sr_{1+2x}Mn_2O_7$ with $x = 0.38$, studied using *in situ* Lorentz transmission electron microscopy. The role of magnetocrystalline anisotropy on the structure of domain walls was elucidated. Upon cooling, the magnetic domain contrast was seen to appear first at the Curie temperature within the *a*-*b* plane. With further reduction in temperature, the change in area fraction of magnetic domains was used to estimate the critical exponent describing the ferromagnetic phase transition. The ferromagnetic phase transition was accompanied by a distinctive nanoscale granular contrast close to the Curie temperature, which we infer to be related to the presence of ferromagnetic nanoclusters in a paramagnetic matrix, which has not yet been reported in bilayer manganites.

DOI: 10.1103/PhysRevB.92.224418 PACS number(s): 75.47.Gk, 75.70.Kw, 75.47.Lx

I. INTRODUCTION

Bilayer manganites such as $La_{2-2x}Sr_{1+2x}Mn_2O_7$ exhibit a rich phase diagram based on their doping level, which includes ferromagnetic (FM), antiferromagnetic (AF), and charge-ordered phases [1,2]. Due to the complex crystal structure, there are several different exchange interactions within these materials that contribute to their behavior. For example the inter-bilayer exchange along the *c* axis is weaker than the intra-bilayer exchange within the *a*-*b* plane, as a result of the intrinsic two-dimensional layered structure [3,4]. These anisotropic exchange interactions along with the competition among orbital, charge, and spin order, as well as lattice distortions, lead to interesting and complex magnetic and transport properties. The double-exchange interaction between the Mn^{3+} and Mn^{4+} ions results in the material undergoing a phase transition from a paramagnetic (PM) insulator to a ferromagnetic (FM) metallic state below the Curie temperature [5]. As a result of this dramatic change in conductivity, the layered manganites exhibit a colossal magnetoresistance (CMR) effect, which has garnered much attention in the past two decades from both a fundamental as well as an applications context.

One of the proposed mechanisms for the CMR effect is that small FM regions, which are connected in a percolative manner [6], form as the material is cooled through the transition temperature. Magnetic interactions and domains in these manganites and related materials have previously been studied using various techniques such as neutron scattering [7,8] and magnetic force microscopy [9], as well as Kerr microscopy [10]. The majority of the research efforts towards understanding the formation of FM domains has been done using reciprocal space and scattering methods. Only recently there have been some efforts towards direct real space visualization of the way in which the small FM regions form and become connected, leading to the formation of FM domains within the material below T_c. Lorentz transmission electron microscopy (LTEM) has also been used to study cubic manganites since it offers high spatial resolution and a direct visualization of the magnetic domains [11–13]. Furthermore with current advanced *in situ* capabilities, LTEM offers unique possibilities to study the magnetic phase transitions as a function of temperature, while simultaneously obtaining information about structural and charge ordering using electron diffraction. Phase-reconstruction methods enable quantitative magnetic induction maps to be obtained that can provide information about the nature of the magnetic domain walls as well as physical parameters such as the exchange stiffness of the sample.

In this work, we have explored the behavior of $La_{2-2x}Sr_{1+2x}Mn_2O_7$ with $x = 0.38$, which has been reported to show a ferromagnetic transition with a Curie temperature of $T_c = 125$ K [14]. At this doping level, the magnetic moments in the unit cell are oriented such that the crystal has a strong easy plane (*a*-*b* plane) anisotropy with $K_u \approx -2.5 \times 10^5$ J/m^3 [15]. Both the Curie temperature and the magnetocrystalline anisotropy are strongly dependent on the doping level for bilayer manganites. For further detailed information regarding the phase diagram of bilayer manganites and the variation of magnetocrystalline anisotropy, we refer the reader to a detailed study by Ling *et al.* [2]. Here we discuss the behavior of the magnetic domains and the relationship between the crystal structure and domain structure together with a derivation of magnetic parameters obtained directly from the nanoscale imaging. Furthermore, we also describe the ferromagnetic phase transition and the observation of a granular nanoscale contrast that provides direct evidence of the coexistence of FM and PM phases in a bilayer manganite.

II. EXPERIMENTAL METHODS

Single crystals of $La_{2-2x}Sr_{1+2x}Mn_2O_7$ with $x = 0.38$, i.e., $La_{1.24}Sr_{1.76}Mn_2O_7$, were synthesized using the floating

*cd@anl.gov

zone method [16]. TEM samples were prepared from these crystals using the focused ion-beam milling method as well as conventional polishing, followed by gentle milling by low-energy Ar^+ ions to improve electron transparency. SQUID magnetometry was performed on the TEM sample and the transition temperature was determined to be $T_c = 125$ K, which is consistent with previous neutron diffraction studies [14]. In order to fully understand the magnetic domain behavior and elucidate the role of magnetocrystalline anisotropy on the formation of domain walls, two samples were fabricated with differing geometry: (1) S1, with the hard axis ($\langle 001 \rangle$) in the plane of the TEM sample, and (2) S2, with the hard axis ($\langle 001 \rangle$) perpendicular to the plane of the TEM sample. Further details about the sample orientation and magnetocrystalline anisotropy are given in the Supplemental Material [17]. The magnetic domain behavior in the samples was then analyzed in the Lorentz TEM mode using a Tecnai F20 transmission electron microscope. Through-focus series of images were acquired with a nominal defocus ranging between $\Delta f = 500$–$1000\ \mu$m. The magnetic domain contrast is only observed in out-of-focus images and not in in-focus images. It should be noted that Lorentz microscopy is only sensitive to magnetization components that are perpendicular to the direction of the electron beam. Additional details about Lorentz microscopy and through-focus imaging are given in the Supplemental Material [17]. The local magnetization was analyzed using the gradient of the phase shift of electrons passing through the sample. This phase shift was recovered using the *transport-of-intensity* equation method [18]. *In situ* experiments were performed using a liquid N_2 stage that is capable of cooling the sample to 90 K, in order to observe the magnetic domain behavior during the magnetic phase transition from the paramagnetic state to the ferromagnetic state.

III. RESULTS

A. Magnetic domain walls

Figure 1(a) shows an underfocused Lorentz TEM image from sample S1 with the hard magnetic axis, $\langle 001 \rangle$, in the plane of the TEM sample. The inset (top right) shows the diffraction pattern viewed along the $\langle 100 \rangle$ zone axis and the orientation of the crystallographic axes in the sample plane is indicated. The sample was cooled to 95 K, which is well below the Curie temperature. As expected, 180° domain walls are present, seen as bright and dark sharp lines, running vertically in the image. The magnetization map within this region was reconstructed from the phase shift of the electrons and is shown as a color map overlaid on the bottom left of the image. The color indicates the direction of magnetization as given by the color wheel. The additional curved lines seen running horizontally in the image are bend contours, which are related to strong electron diffraction effects. This composition of $La_{2-2x}Sr_{1+2x}Mn_2O_7$ is expected to have an easy-plane anisotropy, which means that the magnetization prefers to lie in the *a*-*b* plane. Due to the specific geometry of this TEM sample and its crystallographic orientation, we are observing these *a*-*b* planes edge on, thereby effectively creating a strong uniaxial anisotropy in the TEM sample, with

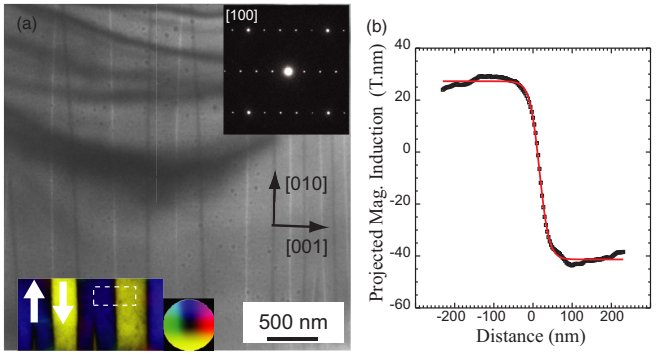

FIG. 1. (Color online) (a) Underfocused LTEM image of sample S1 at 95 K. The top right inset shows the diffraction pattern along the $\langle 100 \rangle$ zone axis and the schematic shows the orientation of the crystallographic axes. The bottom left inset shows the magnetization color map overlaid on the image showing the presence of 180° domain walls. (b) Plot of the projected magnetic induction (black squares) across the domain wall computed by averaging the values shown in the dashed region in (a) and a fit obtained to determine the domain wall width (red).

domain walls separating domains running perpendicular to the $\langle 001 \rangle$ direction. This also manifests itself via the formation of needle-like domains seen in the magnetization color map near the bottom of the image, which is also the edge of the sample. This type of domain is formed in order to minimize the stray field energy. The widths of the domains near the edge and inside the sample are determined by a balance between the domain wall energy and the closure (stray) field energy. The domain pattern observed here is an example of two-phase branching, which refines the domain pattern near an edge [19]. This effect is observed in sample S1 because it has a strong effective uniaxial anisotropy along the $\langle 010 \rangle$ direction resulting in the magnetization lying along only two easy magnetization directions: [010] and [0$\bar{1}$0].

Since the hard axis for magnetization is in the plane of the sample, the domain walls can be expected to be of Bloch type, where the magnetization rotates out-of-plane across the wall. The width of the domain wall can be related to physical constants such as the exchange stiffness and magnetocrystalline anisotropy using the relation $\delta \sim \pi\sqrt{A/|K_u|}$ [19]. Using the classical approximation of spin rotation across a 180° domain wall, the distribution of the in-plane component of the magnetic induction can be approximated using the relation

$$B_y = a + b\tanh\{(x - c)/\delta\}, \tag{1}$$

where a,b,c are constants and δ is the domain wall width. Figure 1(b) shows a plot of the in-plane component of the projected magnetic induction across the domain wall (black squares). The values were averaged over the region showed by dashed lines in Fig. 1(a). A nonlinear least-squares fit to the measured data was performed (shown in red) using Eq. (1), from which the domain wall width was determined to be 24.5 nm. Furthermore, using the value of $K_u = 2.5 \times 10^5$ J/m^3 from the literature [15], a value for the exchange stiffness constant for $La_{1.24}Sr_{1.76}Mn_2O_7$ was determined to be $A = 15.2 \times 10^{-12}$ J/m. This demonstrates that we can determine

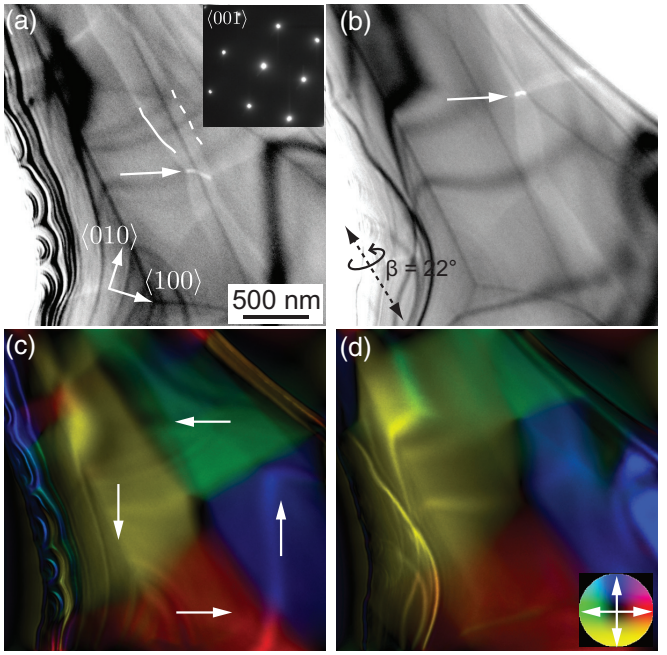

FIG. 2. (Color online) (a) Underfocused LTEM image from sample S2 at 95 K. The inset shows the diffraction pattern obtained along the ⟨001⟩ zone axis and the orientation of the crystallographic axes is shown schematically. (b) Underfocused LTEM image of the same region after tilting the sample by 22° about the axis shown in the figure. (c) and (d) Reconstructed magnetization color map for (a) and (b), respectively. The color wheel indicates the direction of magnetization.

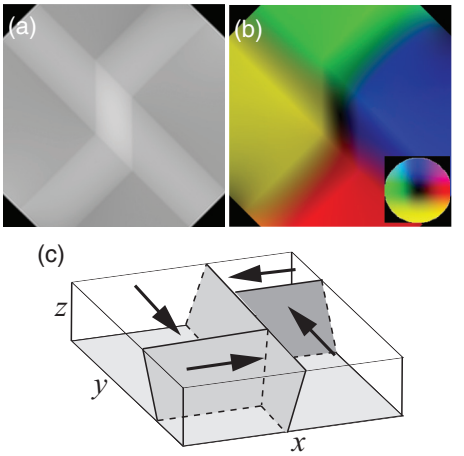

FIG. 3. (Color online) (a) Simulated underfocused LTEM image and (b) the corresponding magnetization color map for a model with inclined domain walls forming a closure domain configuration, as shown schematically in (c).

the magnetic parameters of a material directly using nanoscale imaging. The exchange stiffness constant can in principle be related to the exchange interactions (J_{ex}) in the effective Heisenberg Hamiltonian, but it is dependent on the crystal structure of the material [20]. Moreover, A is a micromagnetic quantity that averages the atomic exchange interactions over several unit cells and requires the knowledge of spin quantum numbers to be able to correlate it with J_{ex}. As such for a bilayer manganite sample with interlayer exchange as well as intralayer exchange, it is difficult to correlate these individual atomic interactions with the micromagnetic measurement.

The magnetic domain structure in sample S2, which has the hard axis of magnetization perpendicular to the plane of the sample, is shown in Fig. 2. Figure 2(a) shows an under-focused LTEM image from this sample. The top-right inset shows the diffraction pattern along the ⟨001⟩ zone axis and the in-plane crystallographic directions are indicated. The domain walls are not seen as sharp lines as they were for sample S1, but now show a broad bandlike contrast as highlighted by the white lines. The width of the bandlike contrast varies from narrow at the edge of the sample to broad inside the sample. In this orientation, the easy plane (a-b) of magnetization is in the plane of the TEM sample, and the surface termination and sample edges lead to formation of a closure domain configuration to minimize the stray fields. This is clearly seen from the colored magnetization map shown in Fig. 2(c). The magnetization direction within each region is close to a ⟨110⟩-type direction. It has previously been estimated from bulk magnetic measurements that although there is an easy-plane anisotropy in $La_{1.24}Sr_{1.76}Mn_2O_7$, there is a small uniaxial anisotropy of about 7×10^3 J/m^3 along the ⟨110⟩ direction [15]. It is interesting to note that at the location where two of the domain walls intersect, a bright white line contrast is observed (indicated by the arrow). The broadening of the domain walls can be attributed to either a large domain wall width or the presence of inclined domain walls. As we have already estimated that the domain wall width for this material is 77 nm from the images of sample S1, this cannot explain the broad contrast extending over a range of 300 nm. Hence we can infer that the domain walls must be inclined with respect to the viewing direction. This was further investigated by tilting the sample to observe the effect on the domain wall contrast. Figure 2(b) shows an underfocused Lorentz TEM image of the same region after tilting by 22° about the axis shown in (b). Figure 2(d) shows the corresponding colored magnetization map. The effective broadening of the domain wall contrast has decreased along with a decrease in the length of the bright white line contrast.

In order to confirm the origin of the contrast, we performed image simulations as shown in Fig. 3. The details of the image simulation are given in the Supplemental Material [17]. Figure 3(a) shows a simulated underfocused image and Fig. 3(b) shows the corresponding colored magnetization map. The magnetic configuration with inclined domain walls (gray) used for these image simulations is shown schematically in Fig. 3(c). There is excellent agreement between the simulated images and the experimental ones in terms of the color contrast for each of the magnetic domains as well as the black region at the center of the magnetization map, corroborating our view that the domain walls observed for this sample are indeed inclined with respect to the viewing direction (∼⟨001⟩). By comparison with the model, we can interpret the features indicated by the solid and dashed lines in Fig. 2(a) as the intersection of the domain wall with the top surface and bottom surface of the TEM sample, respectively.

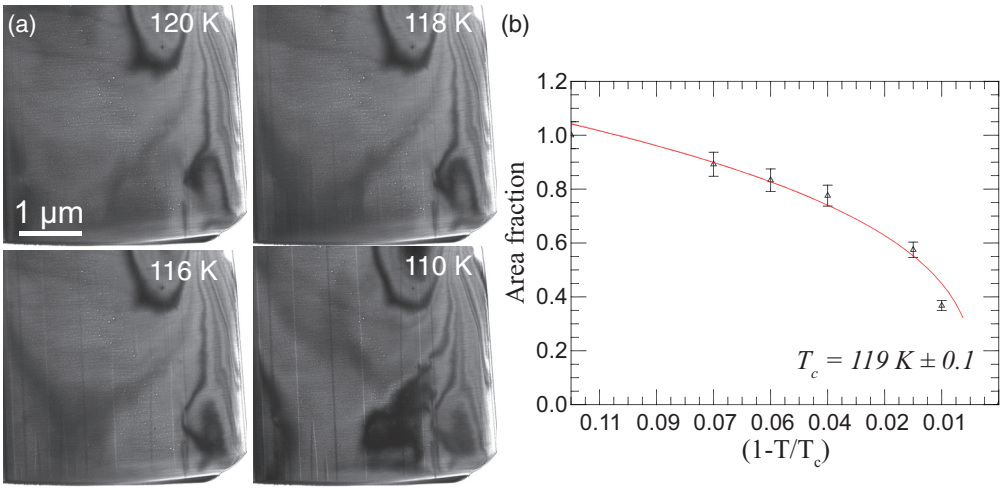

FIG. 4. (Color online) (a) Series of underfocused LTEM images acquired during the cooling of sample S1 from 120 K to 110 K. (b) Plot of the area fraction of magnetic domains as a function of reduced temperature $(1 - T/T_c)$ as calculated from the *in situ* cooling image series (diamonds) and a power-law fit to the data (red line).

B. Ferromagnetic transition

Next we explored the magnetic domain behavior as a function of temperature across the phase transition from paramagnetic to ferromagnetic state for both the sample geometries. Figure 4 shows the phase transition for TEM sample S1 (hard axis in the plane of the sample). At 120 K, there is no magnetic contrast seen in the sample. The observed contrast is only due to electron diffraction. As the temperature decreases from 120 K, the 180° domain walls are seen to nucleate at the edge of the sample (bottom of the images) and then grow across the TEM sample. The first appearance of magnetic domain wall contrast was observed at $T = 118$ K. This temperature is about 7 K lower than the Curie temperature of the same TEM sample as measured from magnetometry to be $T_c = 125$ K. This difference can attributed to the fact that at temperatures very close to T_c, the ferromagnetic domain signal is too weak to be detected using Lorentz TEM. Similar differences between the temperature at which magnetic contrast is observed and the Curie temperature have previously been reported [13,21]. The area fraction of the sample that was ferromagnetic was calculated as a function of temperature from this series of images. This area fraction was measured from the underfocused Lorentz TEM images as the area over which the magnetic domain walls were observed. The area fraction roughly corresponds to the total magnetization of the sample under the assumption that it is uniform through the thickness of the sample. A power-law fit to the area fraction, A (which is representative of the magnetization), and the reduced temperature, $t = (1 - T/T_c)$, using the relation $A = Ct^{\beta}$ was performed with fitting parameters of C, β, and T_c. A least-squares fit yields the exponent, $\beta = 0.34 \pm 0.02$, $C = 2.1 \pm 0.04$, and $T_c = 119.2\,\text{K} \pm 0.1$. The fit was performed for the data in the range of $T = 105$–118 K. Figure 4(b) shows the plot of the measured area fraction as a function of temperature (symbols) together with the power-law best fit to the data (red line). This value of β is close to the literature reported value of $\beta = 0.32$ for a three-dimensional Ising model [22]. Previous reports have determined the value of $\beta = 0.13$ which indicate that the phase transition below T_c is still explained by the 2D Ising model [7]; however a crossover to a three-dimensional Ising model close to T_c has also been suggested [8]. The fitting also suggests a lower value of T_c than that measured from bulk magnetometry. However again this could be related to the fact that the ferromagnetic domain signal is too weak to be detected using Lorentz TEM near T_c.

As for the domain wall structure, a distinctive difference was observed during the phase transition for sample S2 compared with that for S1. Figure 5 shows a series of underfocused Lorentz TEM images during cooling to below T_c. As the sample is cooled, there is no immediate formation

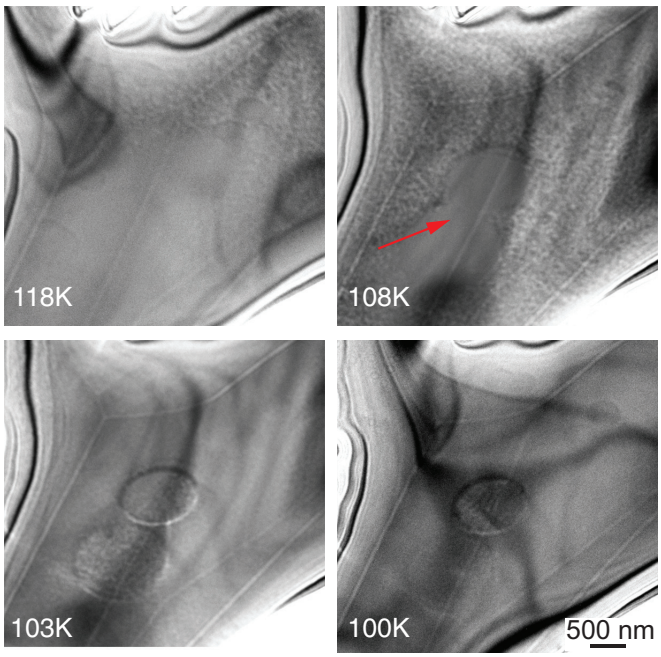

FIG. 5. (Color online) Series of underfocused LTEM images from sample S2 during *in situ* cooling from 120 K to 100 K. The nanoscale granular contrast starts to appear at 118 K and eventually disappears, leaving magnetic domain walls at 100 K.

of magnetic domain walls, but rather the formation of a nanoscale granular contrast starting from $T = 118$ K, which increases in density as the temperature decreases. The granular nanoscale contrast was only observed in the out-of-focus images and not in the in-focus image, indicating that it is magnetic in origin. Eventually these nanoscale magnetic clusters merge together to form magnetic domains separated by domain walls, leading to a decrease in the total number of clusters. Finally at 100 K, most of the nanoscale clusters disappear leaving behind domain walls that form a closure domain configuration to minimize the stray field energy. It should also be noted that at $T = 108$ K, there is a region in the center of the sample marked by a red arrow that does not show any black and white granular contrast related to the nanoscale clusters, although it is surrounded by this contrast. Eventually at $T = 103$ K, the granular contrast is seen inside the region, which slowly disappears by $T =$ 100 K. This suggests that there are local inhomogeneities (for example due to strain in the sample) that can result in a difference in Curie temperature. The effect of such local inhomogeneities is often missed in bulk measurements as they are averaged over the entire sample. However using LTEM, we are able to observe the coexistence of submicron-size regions that are nonferromagnetic in the surrounding ferromagnetic region. Similar coexistence of charge-ordered (insulating) and charge-disordered (metallic FM) domains has been previously observed in $La_{5/8-y}Pr_yCa_{3/8}MnO_3$ [6]. Additionally as the sample was cooled, the bend contour contrast in the TEM sample was seen to change sharply over a narrow temperature range just above the Curie temperature, indicating a change in the strain state of the sample. This can be directly related to the magnetostriction of the sample as it undergoes the phase transition from the PM to FM phase. Note that the bend contour contrast stays stable over the rest of the temperature range analyzed. The abrupt change in volume and the resulting magnetostriction effect at T_c have previously been reported in bilayer manganites and are associated with the insulator-to-metal transition in these materials [23].

Figures 6(a), 6(b), and 6(c) show the underfocused, overfocused, and in-focus Lorentz TEM images, respectively, of the granular contrast for $T = 108$ K. The granular contrast arising from the nanoscale clusters (highlighted by the red circle) shows a distinctive white and black intensity on either side of each cluster. The inset at the top right of Figs. 6(a) and 6(b) shows the magnified view of the region circled in red. This black and white intensity reverses between the underfocused and overfocused images as shown by the plot of normalized intensity in Fig. 6(d), and disappears for the in-focus images. This type of contrast is observed for a spatial distribution of finite objects in the sample that leads to a phase shift of the electron wave passing through it, resulting in the observation of the contrast only in out-of-focus images. Thus the contrast could be related to a distribution of magnetic objects or to effects such as strain related to the phase transition. If the origin of the contrast were crystallographic, i.e., strain, then changes in the bend contour contrast would also be expected. However this was only observed prior to the appearance of the granular contrast as mentioned earlier. We therefore infer that the origin is magnetic and is evidence for the formation of a random distribution of ferromagnetic clusters

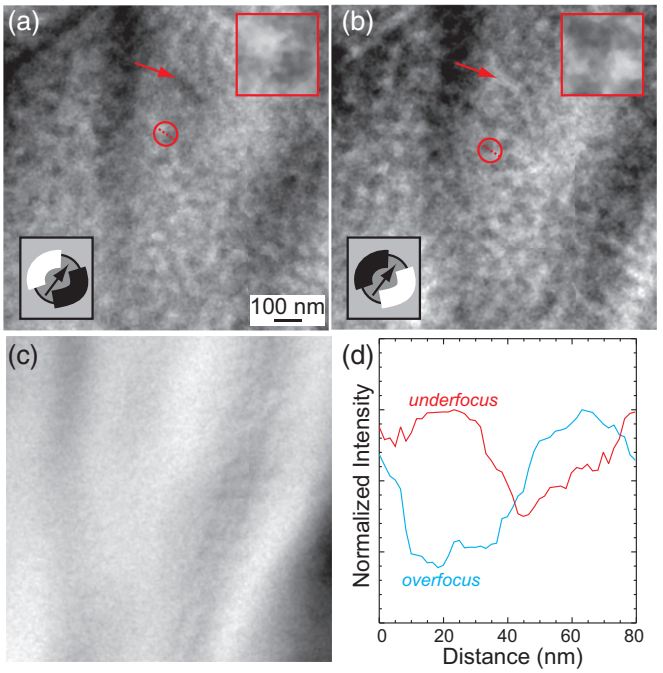

FIG. 6. (Color online) (a)–(c) Underfocused, overfocused, and in-focus LTEM images, respectively, of an area showing the nanoscale granular contrast at 109 K from sample S2. A magnified view of the region in the red circle is shown in the top left inset showing the black and white contrast associated with the nanoclusters. The schematic in the bottom right inset shows the relation between the black and white contrast and the magnetization of the local cluster. (d) Plot of the normalized intensity across the dashed red line in (a) and (b).

in a nonmagnetic matrix. Since the spins of individual atoms within these ferromagnetic clusters are aligned, each cluster can be described as a nanoscale single-domain magnetic object. The expected contrast in the out-of-focus images that is associated with such a single-domain magnetic object is schematically shown in the bottom inset of Figs. 6(a) and 6(b). Further evidence for this interpretation comes from the fact that the nanoclusters eventually merge to form domains. An example of a wall segment that has formed is indicated by the red arrow in Figs. 6(a) and 6(b).

A similar granular contrast of nanoclusters has previously been observed, although only in cubic manganites such as $Nd_{0.5}Sr_{0.5}MnO_3$ [11] and $La_{0.55}Ca_{0.45}MnO_3$ [13]. In both cases, the granular contrast was associated with the presence of ferromagnetic nanoclusters. However, in the case of $Nd_{0.5}Sr_{0.5}MnO_3$, the granular contrast was observed only during the phase transition from the AF phase to FM phase. In the case of $La_{0.55}Ca_{0.45}MnO_3$, the ferromagnetic nanoclusters with an ordered superstructure were seen to form within a matrix that was already ferromagnetic with submicron-size magnetic domains. Here we have observed the formation of these nanoclusters in bilayer manganites during both cooling through the Curie temperature and heating through it, without the presence of a charge-ordered phase or any other form of superstructure. The lack of any structural or long-range charge ordering was confirmed using electron diffraction during the heating and cooling. From the plot of the intensity [Fig. 6(d)], the size of these nanoclusters can be measured as roughly

40 nm (peak-to-peak distance). However, it must be noted that the high defocus value used in these images results in additional magnification. Therefore the true size of these nanoclusters is expected to be smaller than 40 nm. This size is still significantly larger than the lattice spacing in the *a-b* plane of ∼0.4 nm or the inter-bilayer distance of ∼2 nm. This suggests that we are only able to image the clusters once they reach a size at which their net magnetic moment is detectable using Lorentz TEM.

IV. SUMMARY

In summary, we have studied the magnetic domain wall structure in $La_{1.24}Sr_{1.76}Mn_2O_7$ in the ferromagnetic regime and its relation to the crystallography of the sample. Using the freedom to prepare the TEM sample along different crystallographic orientations, we investigated the detailed structure of the domain walls and were able to conclude that fabrication of the TEM sample does not significantly alter the domain wall behavior as compared to the bulk. When the hard axis of magnetization was in the plane of the TEM sample, 180° Bloch walls are observed. By measuring the domain wall width from the nanoscale imaging, we determined the exchange stiffness of the material. In the sample with the hard axis of magnetization perpendicular to the sample plane, we observed broad bandlike contrast for the domain walls. By comparing the experimental images with simulated ones, we were able to conclude that the domain walls are inclined which results in the broadening of the contrast. By analyzing the *in situ* growth of magnetic domains as a function of temperature during cooling, we were able to determine the nature of the ferromagnetic transition by fitting a power law to the magnetization versus temperature data and estimating the critical exponent β to be 0.36. We infer that this corresponds to a crossover to three-dimensional scaling close to T_c. We were also able to visualize the formation of nanoclusters during the phase transition close to $T = T_c$ which showed a direct evidence of coexistence of magnetic and nonmagnetic phases in bilayer manganites. Additionally, we also observed that there are local submicron-scale regions which become ferromagnetic at slightly different temperatures as compared to their surroundings. Both the formation of nanoclusters and submicron-scale regions suggest that this phase transition is percolative in nature. Further detailed image analysis of the nanoclusters to determine their relative size and density as a function of temperature could yield more insights into the details of the phase transition.

Note added. Recent work by Bryant *et al.* [24] reported on imaging the magnetic domain walls as a function of temperature in $La_{1.2}Sr_{1.8}Mn_2O_7$ ($x = 0.40$) using low-temperature magnetic force microscopy. They measured T_c close to 118 K; however, they observed that the magnetic domain walls disappear at about 20 K below T_c. This observation could be related to suppression of the magnetization at the surface which has been previously reported [25]. However, they are only able to observe surface effects and do not report on the formation of magnetic domain walls or the formation of nanoclusters close to T_c.

ACKNOWLEDGMENTS

This work was supported by the U.S. Department of Energy, Office of Science, Basic Energy Sciences, Materials Sciences and Engineering Division. Use of the Center for Nanoscale Materials, an Office of Science user facility, was supported by the U.S. Department of Energy, Office of Science, Office of Basic Energy Sciences, under Contract No. DE-AC02-06CH11357.

[1] D. Argyriou, J. Mitchell, P. Radaelli, H. N. Bordallo, D. E. Cox, M. Medarde, and J. D. Jorgensen, Phys. Rev. B **59**, 8695 (1999).
[2] C. D. Ling, J. E. Millburn, J. F. Mitchell, D. N. Argyriou, J. Linton, and H. N. Bordallo, Phys. Rev. B **62**, 15096 (2000).
[3] Y. Moritomo, A. Asamitsu, H. Kuwahara, and Y. Tokura, Nature (London) **380**, 141 (1996).
[4] T. G. Perring, D. T. Adroja, G. Chaboussant, G. Aeppli, T. Kimura, and Y. Tokura, Phys. Rev. Lett. **87**, 217201 (2001), 0105230.
[5] Y. Konishi, T. Kimura, M. Izumi, M. Kawasaki, and Y. Tokura, Appl. Phys. Lett. **73**, 3004 (1998).
[6] M. Uehara, S. Mori, C. Chen, and S. Cheong, Nature (London) **399**, 560 (1999).
[7] R. Osborn, S. Rosenkranz, D. N. Argyriou, L. Vasiliu-Doloc, J. W. Lynn, S. K. Sinha, J. F. Mitchell, K. E. Gray, and S. D. Bader, Phys. Rev. Lett. **81**, 3964 (1998).
[8] S. Rosenkranz, R. Osborn, J. F. Mitchell, L. Vasiliu-Doloc, J. W. Lynn, and S. K. Sinha, J. Appl. Phys. **87**, 5816 (2000).
[9] Q. Lu, C.-C. Chen, and A. de Lozanne, Science **276**, 2006 (1997).
[10] A. Gupta, G. Gong, G. Xiao, P. Duncombe, P. Lecoeur, P. Trouilloud, Y. Wang, V. Dravid, and J. Sun, Phys. Rev. B **54**, R15629 (1996).
[11] T. Asaka, Y. Anan, T. Nagai, S. Tsutsumi, H. Kuwahara, K. Kimoto, Y. Tokura, and Y. Matsui, Phys. Rev. Lett. **89**, 207203 (2002).
[12] J. Loudon, N. Mathur, and P. Midgley, Nature (London) **420**, 797 (2002).
[13] J. Tao, D. Niebieskikwiat, Q. Jie, M. A. Schofield, L. Wu, Q. Li, and Y. Zhu, Proc. Natl. Acad. Sci. **108**, 20941 (2011).
[14] M. Medarde, J. Mitchell, J. Millburn, S. Short, and J. Jorgensen, Phys. Rev. Lett. **83**, 1223 (1999).
[15] U. Welp, A. Berger, V. K. Vlasko-Vlasov, H. You, K. E. Gray, and J. F. Mitchell, J. Appl. Phys. **89**, 6621 (2001).
[16] J. F. Mitchell, D. N. Argyriou, J. D. Jorgensen, D. G. Hinks, C. D. Potter, and S. D. Bader, Phys. Rev. B **55**, 63 (1997).
[17] See Supplemental Material at http://link.aps.org/supplemental/10.1103/PhysRevB.92.224418 for additional information about the crystal structure, anisotropy direction and sample orientation as well as details of image simulation.
[18] V. V. Volkov, Y. Zhu, and M. De Graef, Micron **33**, 411 (2002).
[19] A. Hubert and R. Schäfer, *Magnetic Domains: The Analysis of Magnetic Microstructures* (Springer, Berlin, 1998).
[20] D. Jiles, *Introduction to Magnetism and Magnetic Materials*, 2nd ed. (CRC press, Boca Raton, 1998).

[21] J. Loudon and P. Midgley, Phys. Rev. Lett. **96**, 027214 (2006).
[22] A. Pelissetto and E. Vicari, Phys. Rep. **368**, 549 (2002).
[23] M. Matsukawa, H. Ogasawara, T. Sasaki, M. Yoshizawa, M. Apostu, R. Suryanarayanan, A. Revcolevschi, K. Itoh, and N. Kobayashi, J. Phys. Soc. Jpn. **71**, 1475 (2002).
[24] B. Bryant, Y. Moritomo, Y. Tokura, and G. Aeppli, Phys. Rev. B **91**, 134408 (2015).
[25] J. W. Freeland, J. J. Kavich, K. E. Gray, L. Ozyuzer, H. Zheng, J. F. Mitchell, M. P. Warusawithana, P. Ryan, X. Zhai, R. H. Kodama, and J. N. Eckstein, J. Phys.: Condens. Matter **19**, 315210 (2007).